


Inertial Migration in a Pressure-Driven Channel Flow: Beyond the Segre-Silberberg Pinch

Prateek Anand¹ and Ganesh Subramanian^{2,*}

¹*International Centre for Theoretical Sciences, Bengaluru-560089, India*

²*Jawaharlal Nehru Centre for Advanced Scientific Research, Bengaluru-560064, India*

 (Received 4 April 2023; revised 15 September 2023; accepted 2 January 2024; published 30 January 2024)

We examine theoretically the inertial migration of a neutrally buoyant rigid sphere in pressure-driven channel flow, accounting for its finite size relative to the channel width (the confinement ratio). For sufficiently large channel Reynolds numbers (Re_c), a small but finite confinement ratio qualitatively alters the inertial lift velocity profiles obtained using a point-particle formulation. Finite size effects lead to new equilibria, in addition to the well-known Segre-Silberberg pinch locations. Consequently, a sphere can migrate to either the near-wall Segre-Silberberg equilibria, or the new stable equilibria located closer to the channel centerline, depending on Re_c and its initial position. Our findings are in accord with recent experiments and simulations, and have implications for passive sorting of particles based on size, shape, and other physical characteristics, in microfluidic applications.

DOI: [10.1103/PhysRevLett.132.054002](https://doi.org/10.1103/PhysRevLett.132.054002)

Inertial migration of neutrally buoyant spheres in pipe flow, to an annular location between the centerline and walls, was first observed by Segre and Silberberg [1–3], the location termed the Segre-Silberberg annulus (henceforth, SS annulus or equilibria). Equilibria arising from inertial lift forces have since been exploited in microfluidic applications [4–8]. The first theoretical explanations of the phenomenon were for pressure-driven channel flow (the plane Poiseuille profile) [9,10], and based on the inertial lift on a sphere for $Re_p, Re_c \ll 1$, Re_p and Re_c being the particle and channel Reynolds numbers, respectively [11]. The pair of zero crossings of the $O(Re_p)$ lift profile, symmetrically located about the centerline, corresponded to the SS equilibria. Calculations were later extended to $Re_c \gtrsim O(1)$ [12,13], with the SS equilibria starting at a location intermediate between the walls and centerline for $Re_c \ll 1$, and moving wallward with increasing Re_c . An analogous dependence on Reynolds number was predicted for the SS annulus in pipe flow [14], pointing to the similar physics governing migration in the two configurations.

Later experiments [15], while confirming the original observations [1–3], revealed an additional inner annulus, this being the only equilibrium location beyond a certain Re_c . The calculations above [9,10,12,13] use a point-particle approximation, and predict only the pair of SS equilibria in plane Poiseuille flow, and the SS annulus alone in pipe flow [14], regardless of Re_c . The inner annulus was therefore speculated to arise from finite-size effects [15]. Although initially regarded as a transient feature [16], recent experiments [17] have confirmed the inner annulus to be a stable equilibrium, leading to the following migration scenario: all spheres focus onto the SS annulus

at low Re_c (Regime A); for Re_c above a threshold, spheres focus onto either the SS annulus or the inner annulus depending on their initial location (Regime B); spheres focus solely onto the inner annulus beyond a second threshold (Regime C). The threshold Re_c 's demarcating different regimes decrease with increasing confinement ratio (λ), defined as the ratio of the sphere radius a to channel width H (or pipe radius). This scenario is qualitatively confirmed by simulations [18,19], although the parameter ranges explored in these studies are restricted.

Herein, we move beyond earlier point-particle formulations, and theoretically examine inertial migration in plane Poiseuille flow for small but finite λ , with $Re_c = V_{\max}H/\nu$ being arbitrary; V_{\max} here is the centerline speed, and ν the kinematic viscosity of the suspending fluid. $Re_p = \lambda^2 Re_c$ is assumed small, allowing analytical progress based on a leading order Stokesian approximation. For large Re_c , the $O(\lambda Re_p)$ finite-size contribution is shown to qualitatively alter the point-particle ($\lambda = 0$) inertial lift profiles in a manner consistent with the recent studies above. Specifically, a new pair of equilibria, closer to the centerline, emerges beyond a threshold Re_c , even for $Re_p \ll 1$. We provide a complete characterization of migration scenarios in the $\lambda - Re_c$ plane.

For a neutrally buoyant torque-free rigid sphere in plane Poiseuille flow, at a distance d from the lower wall (see Fig. 1), use of the reciprocal theorem leads to the following expression for the inertial lift velocity (scaled by $V_{\max}\lambda$) [20–22]:

$$V_p = -Re_p \int_{V^F} \mathbf{u}^{(2)} \cdot \left(\mathbf{u}^{(1)} \cdot \nabla \mathbf{u}^{(1)} + \mathbf{u}^{(1)} \cdot \nabla \mathbf{u}^\infty + \mathbf{u}^\infty \cdot \nabla \mathbf{u}^{(1)} \right) dV, \quad (1)$$

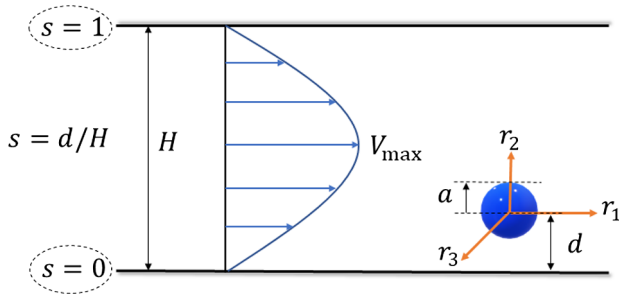


FIG. 1. A neutrally buoyant sphere of radius a in pressure-driven flow through a channel of width H .

the integration being over the fluid volume V^F . The inertial acceleration terms in the integrand involve $\mathbf{u}^{(1)}$, the disturbance velocity field due to the aforesaid neutrally buoyant sphere at a given Re_c , while $\mathbf{u}^{(2)}$ is the Stokesian test velocity field due to the same sphere translating under a unit force, normal to the channel walls, in an otherwise quiescent fluid. $\mathbf{u}^\infty = (\beta r_2 + \lambda \gamma r_2^2 - \lambda \gamma/3)\mathbf{1}_1$ is the ambient Poiseuille flow in a reference frame translating with the sphere, r_2 being the gradient coordinate relative to the sphere center [23]; $\beta = 4(1 - 2s)$ and $\gamma = -4$ denote the ambient shear rate and curvature.

For Re_p small, on using the asymptotic forms of $\mathbf{u}^{(1)}$ and $\mathbf{u}^{(2)}$ for $a \ll r \ll \min(H, H\text{Re}_c^{\frac{1}{2}})$, r being the distance from the sphere, the integral in (1) is found to diverge due to the linearized inertial terms ($\mathbf{u}^{(1)} \cdot \nabla \mathbf{u}^\infty$, $\mathbf{u}^\infty \cdot \nabla \mathbf{u}^{(1)}$), implying that the dominant contributions to V_p arise from scales of $O(H)$, and of $O(H\text{Re}_c^{\frac{1}{2}})$ or larger, for $\text{Re}_c \ll 1$ and $\gg 1$, respectively [20]. Hence, neglecting the finite sphere size and nonlinear inertial terms ($\mathbf{u}^{(1)} \cdot \nabla \mathbf{u}^{(1)}$), one obtains the point-particle approximation [20],

$$V_p = -\text{Re}_p \int_{V^F + V^P} \mathbf{u}_{\text{St}} \cdot (\mathbf{u}_{\text{str}}^{\text{NS}} \cdot \nabla \mathbf{U}^\infty + \mathbf{U}^\infty \cdot \nabla \mathbf{u}_{\text{str}}^{\text{NS}}) dV, \quad (2)$$

examined earlier [9,10,12,13]. The integration is now over the total volume between channel walls, with $\mathbf{u}^{(2)}$ approximated by \mathbf{u}_{St} , the velocity field due to a Stokeslet oriented perpendicular to the walls. $\mathbf{u}^{(1)}$ is replaced by $\mathbf{u}_{\text{str}}^{\text{NS}}$, the solution of the linearized Navier-Stokes equations driven by a stresslet proportional to the plane Poiseuille rate of strain tensor, $(\beta/2)(\mathbf{1}_1 \mathbf{1}_2 + \mathbf{1}_2 \mathbf{1}_1)$; $\mathbf{1}_2$ being the gradient-aligned unit vector. $\mathbf{U}^\infty = (\beta r_2 + \lambda \gamma r_2^2)\mathbf{1}_1$ is the Poiseuille flow in a reference frame moving with the fluid at the sphere center, and omits the smaller ambient-curvature contribution in \mathbf{u}^∞ .

We now add and subtract the point-particle contribution [given by (2)], in (1), recognizing that the difference between the exact integral and (2), corresponding to finite-size contributions, comprises (i) the nonlinear inertial terms, (ii) the short-ranged component of the linearized

inertial terms neglected in (2), and (iii) the particle volume (V^P) contribution. All of these are dominated by scales of $O(a)$, and the lift velocity may therefore be written as [20]

$$V_p(s) = -\text{Re}_p \int_{V^F + V^P} \mathbf{u}_{\text{St}} \cdot (\mathbf{u}_{\text{str}}^{\text{NS}} \cdot \nabla \mathbf{U}^\infty + \mathbf{U}^\infty \cdot \nabla \mathbf{u}_{\text{str}}^{\text{NS}}) dV \\ + \lambda \text{Re}_p \left[- \int_{V^\infty} \mathbf{u}_i^{(2)} \cdot (\mathbf{u}_{s,i}^{(1)} \cdot \nabla \mathbf{u}_{s,i}^{(1)}) dV \right. \\ - \int_{V^\infty} \left[\mathbf{u}_i^{(2)} \cdot (\mathbf{u}_{s,i}^{(1)} \cdot \nabla \mathbf{u}^\infty + \mathbf{u}^\infty \cdot \nabla \mathbf{u}_{s,i}^{(1)}) \right. \\ \left. \left. - \mathbf{u}_{\text{St},i} \cdot (\mathbf{u}_{\text{str},i} \cdot \nabla \mathbf{U}^\infty + \mathbf{U}^\infty \cdot \nabla \mathbf{u}_{\text{str},i}) \right] dV \right. \\ \left. + \int_{V^P} \mathbf{u}_{\text{St},i} \cdot (\mathbf{u}_{\text{str},i} \cdot \nabla \mathbf{U}^\infty + \mathbf{U}^\infty \cdot \nabla \mathbf{u}_{\text{str},i}) dV \right], \quad (3)$$

where the terms within square brackets are the finite-size contributions. The dominance of scales of $O(a)$ implies that the integration for the first two finite-size terms is over the unbounded fluid domain (V^∞) outside the sphere. Thus, $\mathbf{u}_i^{(2)}$ is the Stokesian disturbance due to a sphere translating under a gradient-aligned unit force, and $\mathbf{u}_{s,i}^{(1)}$ is that due to a force-free torque-free sphere in plane Poiseuille flow, both in an unbounded domain; $\mathbf{u}_{\text{St},i}$ and $\mathbf{u}_{\text{str},i}$ denote the unbounded-domain Stokeslet and stresslet fields [23].

The dependence of the point-particle contribution on H amounts to an Re_c dependence (via $\mathbf{u}_{\text{str}}^{\text{NS}}$) in nondimensional terms, and the first integral in (3) is thus of the form $\text{Re}_p F_1(s, \text{Re}_c)$, with F_1 determined semianalytically for $\text{Re}_c \ll 1$ [9,10,21], and numerically for $\text{Re}_c \gtrsim O(1)$ [12,13,21]. The irrelevance of H for the finite-size integrals implies that the expression within square brackets, in (3), is only a function of s . The simple domain of integration (V^∞ or V^P) leads to it being evaluable in closed form [20], and (3) reduces to

$$V_p(s) = \text{Re}_p \left[F_1(s, \text{Re}_c) + \lambda \frac{1141(1 - 2s)}{216} \right], \quad (4)$$

with $F_1(s, \text{Re}_c)$ computed using a shooting method [12,13,21]. The two terms in (4) are, respectively, the leading contributions in the outer- and inner-region expansions within a matched asymptotic expansions framework [24].

Figure 2(a) shows the point-particle lift profiles, for different Re_c 's, over the lower half-channel (due to anti-symmetry about the centerline). In addition to wallward movement of the lone zero crossing (SS equilibrium), the lift at a fixed location, not close to the wall [25], is seen to decrease in magnitude sharply with increasing Re_c [13]. This reflects weakened particle-wall interactions when the walls recede beyond the inertial screening length of $O(H\text{Re}_c^{\frac{1}{2}})$. Apart from the overall decrease in magnitude,

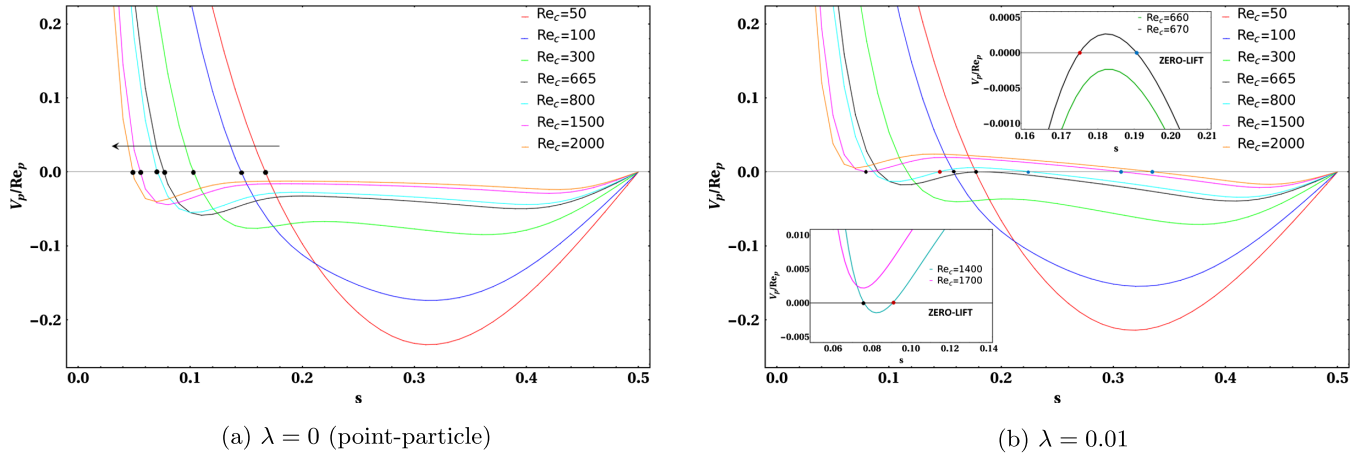


FIG. 2. Inertial lift profiles in the lower half-channel for $Re_c \in [50, 2000]$: (a) $\lambda = 0$ [point-particle profile $F_1(s, Re_c)$]; (b) $\lambda = 0.01$. The arrow in (a) shows the movement of the SS equilibrium with increasing Re_c . The black, red, and blue symbols in (b) denote the SS, unstable and stable equilibria, respectively; the insets in (b) provide a magnified view of the saddle-node bifurcations at $Re_{c_1}^{\text{threshold}} \approx 665$ and $Re_{c_2}^{\text{threshold}} \approx 1500$.

the profile also changes shape, with an intermediate concave-downward portion emerging for $Re_c \gtrsim 300$. An analogous scenario prevails for pipe flow, albeit with the lift being smaller at the same Re_c [14,17].

The changes in the point-particle contribution above imply that the finite-size contribution in (4), although $O(\lambda)$ smaller for $Re_c \ll 1$, becomes comparable for sufficiently large Re_c [26]. This is seen in Fig. 2(b), which shows the lift profiles, for $\lambda = 0.01$, for the Re_c 's in Fig. 2(a). For $Re_c = 50$, the lift profile and the SS equilibrium are only marginally affected. In contrast, for $Re_c = Re_{c_1}^{\text{threshold}}$ (≈ 665 for $\lambda = 0.01$), while the SS equilibrium (expectedly) has moved closer to the walls, a pair of stable and unstable equilibria appear between it and the centerline via a saddle-node bifurcation; the unstable equilibrium demarcating the basins of attraction of the SS and inner stable equilibria. The bifurcation arises due to finite-size effects causing the negative curvature region in the point-particle profile to cross the zero-lift line [upper inset, Fig. 2(b)]. As Re_c increases to 800, the unstable equilibrium moves toward the SS equilibrium even as both move wallward, while the inner stable equilibrium moves toward the centerline. A second bifurcation at $Re_c = Re_{c_2}^{\text{threshold}}$ (≈ 1500 for $\lambda = 0.01$) leads to the latter equilibrium being the only one in the half-channel for larger Re_c [lower inset, Fig. 2(b)]. Note that for $Re_c \in [50, 2000]$, $\lambda = 0.01$, as in Fig. 2(b), $Re_p \in [0.005, 0.2]$, consistent with the assumption of weak fluid inertial effects on scales of $O(a)$.

Figure 3(a) plots the equilibrium loci, identified above, as a function of Re_c . The SS branch starts at $s_{\text{eq}} \approx 0.19$ [the SS equilibrium, $s_{\text{eq}} = 0.182$, modified to $O(\lambda)$] for $Re_c \ll 1$, moving to smaller s with increasing Re_c . The inner stable equilibrium emerges discontinuously at $s_{\text{eq}} \approx 0.18$ for $Re_c \approx 665$, moving to larger s thereafter ($s_{\text{eq}} \approx 0.09$ for the SS equilibrium at this Re_c). The loci of

the SS and inner equilibria appear as sequences of black and blue dots, respectively, with the unstable equilibrium locus connecting the two shown as a sequence of red dots. The fold that develops in the interval $Re_c \in (665, 1500)$, bracketed by the two saddle-node bifurcations, implies a hysteresis [28]. A quasistatic experimental protocol of increasing flow rate will lead to spheres remaining at the SS equilibrium until $Re_c \approx 1500$, at which point they will jump onto the stable branch closer to the centerline. In contrast, for a decreasing flow rate, spheres will remain at the inner stable equilibrium down to $Re_c \approx 665$, before jumping back to the SS branch.

A behavior analogous to that in Fig. 3(a) occurs for smaller λ , with the two Re_c thresholds increasing with decreasing λ . However, the equilibrium loci undergo a qualitative change as λ increases. To see this, note that the SS equilibrium, in the point-particle framework, emerges from a balance between an $O(\beta\gamma)$ curvature-induced contribution driving migration away from the centerline, and an $O(\beta^2)$ wall-induced repulsion. Both contributions arise due to inertial forces on scales of $O(H)$ for $Re_c \ll 1$ [9,21], and decrease with increasing Re_c . The $O(\beta^2)$ contribution decreases faster, leading to wallward movement of the SS equilibrium. Finite-size effects lead to an additional $O(\lambda\beta\gamma)$ curvature-induced contribution, on scales of $O(a)$, that drives migration toward the centerline [20]. The opposing signs of the point-particle and finite-size curvature-induced contributions weaken the wallward movement of the SS equilibrium for larger λ . The result is seen in the equilibrium locus for $\lambda = 0.025$ in Fig. 3(b). The region of multiple equilibria is now absent—the SS equilibrium smoothly transitions from an initial wallward to a subsequent centerward movement across $Re_c \approx 200$.

By identifying equilibrium loci as a function of Re_c , for different λ , a “phase diagram” of migration scenarios in the

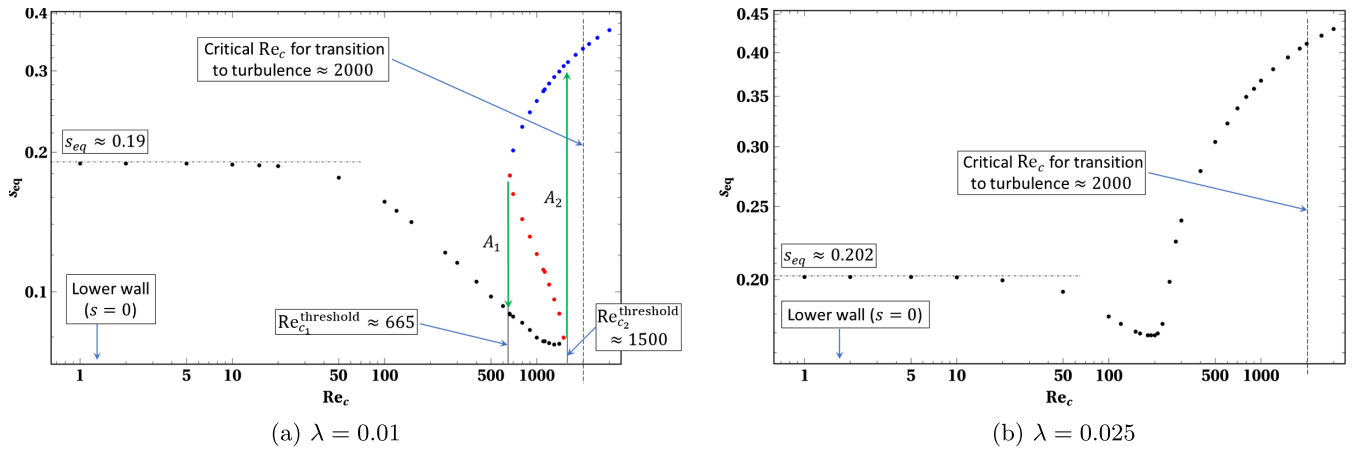


FIG. 3. Inertial equilibrium loci for (a) $\lambda = 0.01$ and (b) $\lambda = 0.025$; black, blue, and red dots denote the SS, and the inner stable and unstable equilibria, respectively. The interval of multiple equilibria, $\text{Re}_c \in (665, 1500)$ in (a), leads to hysteretic jumps in the equilibrium location marked by green arrows (A_1 : $s_{\text{eq}} \equiv 0.179 \rightarrow 0.09$ and A_2 : $s_{\text{eq}} \equiv 0.08 \rightarrow 0.31$). Vertical dashed lines in (a) and (b) denote the laminar-turbulent transition.

$\lambda - \text{Re}_c$ plane is constructed in Fig. 4, highlighting three distinct regions. Region ①, below the red curve but outside the (gray) shaded region, contains lift profiles with a single stable off-center equilibrium in the half-channel. Region ② (the shaded region) contains profiles with two stable equilibria separated by an intervening unstable one. The upper and lower boundaries of this region are determined by the pair of turning points (saddle-node bifurcations) on the equilibrium locus—these were identified in Fig. 3(a) for $\lambda = 0.01$. The boundaries end in a cusp ($\lambda^{\text{critical}}, \text{Re}_c^{\text{critical}} \equiv (0.0216, 296)$)—bottom left inset, Fig. 4 [33,34]. Along either a vertical or a horizontal line, the latter corresponding to an experimental path of changing flow rate, Region ② mediates a discontinuous transition from the SS equilibrium to the inner stable equilibrium. Region ③, above the red curve, includes lift profiles with the centerline as the only stable equilibrium. The centerline is always an equilibrium by symmetry, albeit an unstable one in Regions ① and ②. Insets (a)–(d) in Fig. 4 depict lift profiles consistent with the aforementioned description.

The black dot-dashed line in Fig. 4, corresponding to $\text{Re}_p = 1$, may be regarded as a rough threshold above which the present results may no longer be valid. The region of multiple equilibria and associated hysteretic transitions lie well within this threshold. A second factor limiting the observability of Region ② is the laminar-turbulence transition. Plane Poiseuille flow transitions subcritically to turbulence at $\text{Re}_c \sim O(2000)$ [35], this being marked by dashed vertical lines in both Figs. 3(a) and 3(b), and Fig. 4. The region of multiple equilibria in Fig. 4 appears well before the transition.

While the migration pattern for fixed λ , implied by Fig. 4, is in qualitative agreement with studies quoted at the beginning [15–19], the inner annulus in these studies is observed for higher $\lambda (\gtrsim 0.05)$ and for $\text{Re}_p \gtrsim O(1)$ —see

hatched region in Fig. 4. The absence of multiple equilibria for smaller λ is likely due to the $O(\lambda^{-3})$ development length [15], needed for a steady particle distribution, being larger than the pipe length used. Notwithstanding differences between the pipe and channel geometries, experiments with longer pipes should lead to the hatched region in Fig. 4 extending down to smaller λ . There remains the provocative question of how the secondary finite- Re_p region of multiple equilibria (the hatched region mentioned above), connects to the theoretical small- Re_p one (Region ②).

Apart from the fundamental significance of our findings, in terms of enriching the inertial migration landscape, and providing an explanation for recent experiments and computations, Fig. 4 may be leveraged toward sorting in microfluidic applications. The simplest scenario pertains to

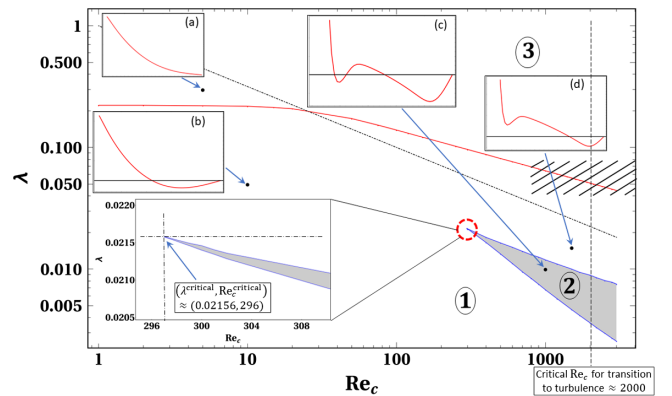


FIG. 4. Migration scenarios in the $\lambda - \text{Re}_c$ plane. Top four insets show inertial lift profiles for the following (λ, Re_c) : (a) (0.3, 5), (b) (0.05, 10), (c) (0.01, 1000), (d) (0.015, 1500); bottom left inset shows the neighborhood of the cusp. The hatched region corresponds to parameter ranges covered in earlier studies [15–19].

spheres of two different sizes, corresponding to confinement ratios λ_1 and λ_2 ($> \lambda_1$). An experimental protocol of changing flow rate (Re_c), for a bidisperse suspension of these particles, would appear as a pair of horizontal lines in Fig. 4, the upper one corresponding to λ_2 . With increasing flow rate, separation would be achieved at an Re_c when the point on the λ_2 line is above Region $\textcircled{2}$ (after crossing it to the right), with the one on the λ_1 line directly below. At this Re_c , larger spheres focus onto the near-centerline stable equilibria, with smaller ones focusing onto the near-wall SS equilibria. If the point on the λ_1 line lies within, rather than below, Region $\textcircled{2}$ (as is the case when λ_2/λ_1 is not far from unity), partial separation will be achieved with smaller spheres focusing onto both the SS and inner equilibria.

The implications of the near-centerline stable equilibria go well beyond the size-sorting scenario above. The dependence of these equilibria on inertial forces, on scales of order the sphere radius, implies a generic sensitivity to detailed characteristics of the suspended microstructure. These include shape parameters for anisotropic rigid particles [36], the viscosity ratio, and capillary number for drops [37–39], and nondimensional parameters based on the membrane viscosity and interfacial elastic moduli for elastic microstructures such as vesicles, capsules, or red blood cells. The analog of Region $\textcircled{2}$ for deformed drops, for instance, will allow for separation based on both drop size and viscosity ratio. It is of interest, in future, to quantitatively determine the relevant migration phase diagrams, which would enable rational design of passive sorting protocols.

*Corresponding author: sganesh@jncasr.ac.in

- [1] G. Segre and A. Silberberg, Radial particle displacements in poiseuille flow of suspensions, *Nature (London)* **189**, 209 (1961).
- [2] G. Segre and A. J. Silberberg, Behaviour of macroscopic rigid spheres in Poiseuille flow Part 1. Determination of local concentration by statistical analysis of particle passages through crossed light beams, *J. Fluid Mech.* **14**, 115 (1962).
- [3] G. Segre and A. Silberberg, Behaviour of macroscopic rigid spheres in Poiseuille flow Part 2. Experimental results and interpretation, *J. Fluid Mech.* **14**, 136 (1962).
- [4] D. Di Carlo, D. Irimia, R. G. Tompkins, and M. Toner, Continuous inertial focusing, ordering, and separation of particles in microchannels, *Proc. Natl. Acad. Sci. U.S.A.* **104**, 18892 (2007).
- [5] D. Di Carlo, Inertial microfluidics, *Lab Chip* **9**, 3038 (2009).
- [6] H. Amini, W. Lee, and D. Di Carlo, Inertial microfluidic physics, *Lab Chip* **14**, 2739 (2014).
- [7] P. Paie, F. Bragheri, D. Di Carlo, and R. Osellame, *Microsyst. Nanoeng.* **3**, 1 (2017).
- [8] M. Li, M. van Zee, K. Goda, and D. Di Carlo, Size-based sorting of hydrogel droplets using inertial microfluidics, *Lab Chip* **18**, 2575 (2018).
- [9] B. P. Ho and L. G. Leal, Inertial migration of rigid spheres in two-dimensional unidirectional flows, *J. Fluid Mech.* **65**, 365 (1974).
- [10] P. Vasseur and R. G. Cox, The lateral migration of a spherical particle in two-dimensional shear flows, *J. Fluid Mech.* **78**, 385 (1976).
- [11] Re_c is the Reynolds number based on the relevant macroscopic scale, either the channel width or the pipe diameter.
- [12] J. A. Schonberg and E. J. Hinch, Inertial migration of a sphere in Poiseuille flow, *J. Fluid Mech.* **203**, 517 (1989).
- [13] E. S. Asmolov, The inertial lift on a spherical particle in a plane Poiseuille flow at large channel Reynolds number, *J. Fluid Mech.* **381**, 63 (1999).
- [14] J. P. Matas, J. F. Morris, and E. Guazzelli, Lateral force on a rigid sphere in large-inertia laminar pipe flow, *J. Fluid Mech.* **621**, 59 (2009).
- [15] J. P. Matas, J. F. Morris, and É. Guazzelli, Inertial migration of rigid spherical particles in Poiseuille flow, *J. Fluid Mech.* **515**, 171 (2004).
- [16] Y. Morita, T. Itano, and M. Sugihara-Seki, Equilibrium radial positions of neutrally buoyant spherical particles over the circular cross-section in Poiseuille flow, *J. Fluid Mech.* **813**, 750 (2017).
- [17] S. Nakayama, H. Yamashita, T. Yabu, T. Itano, and M. Sugihara-Seki, Three regimes of inertial focusing for spherical particles suspended in circular tube flows, *J. Fluid Mech.* **871**, 952 (2019).
- [18] X. Shao, Z. Yu, and B. Sun, Inertial migration of spherical particles in circular Poiseuille flow at moderately high Reynolds numbers, *Phys. Fluids* **20**, 103307 (2008).
- [19] T. W. Pan, A. Li, and R. Glowinski, Numerical study of equilibrium radial positions of neutrally buoyant balls in circular Poiseuille flows, *Phys. Fluids* **33**, 033301 (2021).
- [20] See Supplemental Material at <http://link.aps.org/supplemental/10.1103/PhysRevLett.132.054002> for algebraic details of the calculation procedure.
- [21] P. Anand and G. Subramanian, Inertial migration of a neutrally buoyant spheroid in plane Poiseuille flow, *J. Fluid Mech.* **974**, A39 (2023).
- [22] P. Anand and G. Subramanian, Inertial migration of a sphere in plane Couette flow, *J. Fluid Mech.* **A33**, 977 (2023).
- [23] S. Kim and S. J. Karrila, *Microhydrodynamics: Principles and Selected Applications* (Courier Corporation, Dover, New York, 2013).
- [24] This identification ensures that neglected higher order terms are asymptotically small in relation to those in (4), in turn implying that their inclusion will not lead to new equilibria. The identification also implies that the contributions in (4) arise from mutually exclusive portions of the fluid domain [outer region: $r \gtrsim \min(H, HRe_c^{-\frac{1}{2}})$; inner region: $r \sim O(a)$], with there is no constraint on their relative magnitudes.
- [25] The point-particle lift velocity tends (in magnitude) to 1.52 in plane Poiseuille flow [21] and 0.095 in plane Couette flow [22], independent of Re_c , on approach toward either wall.
- [26] The analog of our finite-size contribution, for a square duct, has been calculated by [27]. However, the point-particle contribution calculated by the authors was based on a

- Stokesian approximation ($Re_c \ll 1$), precluding the creation of new lift-force-induced equilibria.
- [27] K. Hood, S. Lee, and M. Roper, Inertial migration of a rigid sphere in three-dimensional Poiseuille flow, *J. Fluid Mech.* **765**, 452 (2015).
- [28] A hysteresis arises only in the absence of stochastic fluctuations, or for short channels. Either weak Brownian motion [29–31], or pair-hydrodynamic interactions [32] will eliminate hysteretic behavior.
- [29] L. G. Leal and E. J. Hinch, The effect of weak Brownian rotations on particles in shear flow, *J. Fluid Mech.* **46**, 685 (1971).
- [30] V. Dabade, N. K. Marath, and G. Subramanian, The effect of inertia on the orientation dynamics of anisotropic particles in simple shear flow, *J. Fluid Mech.* **791**, 631 (2016).
- [31] N. K. Marath and G. Subramanian, The effect of inertia on the time period of rotation of an anisotropic particle in simple shear flow, *J. Fluid Mech.* **830**, 165 (2017).
- [32] A. Okagawa, R. G. Cox, and S. G. Mason, The kinetics of flowing dispersions. VI. Transient orientation and rheological phenomena of rods and discs in shear flow, *J. Colloid Interface Sci.* **45**, 303 (1973).
- [33] E. C. Zeeman, Catastrophe theory, *Sci. Am.* **234**, No. 4, 65 (1976).
- [34] P. Dubey, A. Roy, and G. Subramanian, Linear stability of a rotating liquid column revisited, *J. Fluid Mech.* **933**, A55 (2022).
- [35] V. C. Patel and M. R. Head, Some observations on skin friction and velocity profiles in fully developed pipe and channel flows, *J. Fluid Mech.* **38**, 181 (1969).
- [36] M. Masaeli, E. Sollier, H. Amini, W. Mao, K. Camacho, N. Doshi, S. Mitragotri, A. Alexeev, and D. Di Carlo, Continuous Inertial Focusing and Separation of Particles by Shape, *Phys. Rev. X* **2**, 031017 (2012).
- [37] P. H. Chan and L. Leal, The motion of a deformable drop in a second-order fluid, *J. Fluid Mech.* **92**, 131 (1979).
- [38] Saeed Mortazavi and G. Tryggvason, A numerical study of the motion of drops in Poiseuille flow. Part 1. Lateral migration of one drop, *J. Fluid Mech.* **411**, 325 (2000).
- [39] A. J. Griggs, A. Z. Zinchenko, and R. H. Davis, Low-Reynolds-number motion of a deformable drop between two parallel plane walls, *Int. J. Multiphase Flow* **33**, 182 (2007).